JOURNAL OF GEOPHYSICAL RESEARCH, VOL. 99, NO. C5, PAGES 9705–9723, MAY 15, 1994

The dependence of microwave backscatter from the sea on illuminated area: Correlation times and lengths

William J. Plant
Applied Physics Laboratory, College of Ocean and Fishery Sciences, University of Washington, Seattle

Eugene A. Terray and Robert A. Petitt, Jr.
Woods Hole Oceanographic Institution, Woods Hole, Massachusetts

William C. Keller[1]
Naval Research Laboratory, Washington, D.C.

Abstract. During the Synthetic Aperture Radar (SAR) and X band Ocean Nonlinearities–Forschungsplattform Nordsee experiment, we mounted two continuous wave microwave systems on an elevator on the German Research Platform Nordsee for the purpose of investigating the dependence of microwave backscatter from the sea surface on illuminated area. The two systems operated at X and Ka bands (10 and 35 GHz) and collected HH and VV polarized backscattered signals simultaneously. The elevator system allowed us to vary the altitude of the two microwave systems above the sea surface from 7.5 to 27 m, always in the far field of the antennas. Most data were collected at a 45° incidence angle, which implied that the Ka band system illuminated areas from 0.4 to 6.0 m^2 while the X band system viewed spots between 2.9 and 41.3 m^2. We examined the dependence of the normalized radar cross section (σ_0), its variance, and the bandwidth of the Doppler spectrum on illuminated areas. We were unable to detect any dependence of σ_0 on area but found a definite decrease in its variance as area increased. At X band the variance divided by the square of σ_0, the normalized variance, decreased from values near 12 for small areas to values near 2 for large areas. At Ka band, corresponding values were 40 and 2. The normalized variance was always slightly larger for HH polarization. By fitting the area dependence of the normalized variance to available theory, we deduce that correlation lengths are on the order of 10 times the microwave wavelength at both X and Ka band. Values for the normalized variance of an elementary scattering facet were also inferred and are presented in this paper. From the Doppler bandwidths we obtained radial velocity spreads over the illuminated areas and found that they agreed well at X and Ka band. These velocity spreads, which are inversely proportional to the correlation time of the backscatter, increased rapidly with illuminated area for small areas but tended to level off to values of about 0.5 m s^{-1} at large areas. This implies a decorrelation time for large illuminated areas of about 10 ms at X band and 3 ms at Ka band but somewhat larger values for small areas. The dependence of the velocity spread was found to be well explained by theory if an intrinsic velocity spread of 0.07 m s^{-1} was used to represent scatterer lifetime effects.

1. Introduction

Microwave backscatter from the sea surface varies rapidly in both space and time but quantitative measurements of how much it varies and on what space scales and timescales are very scarce. *Pidgeon* [1967] has shown that sea backscatter must decorrelate over distances less than the pulse width he used, but that width was 15 m or more. Conventional wisdom holds that correlation times at X band are about 10 ms but recognizes this to be an imprecise value. The value is necessarily imprecise because it is based on observations of Doppler bandwidths that are known to depend on the area illuminated and the state of the sea [*Plant and Keller*, 1990]. Finally, much of our knowledge of the variance of the backscatter comes either from theory [*Fischer*, 1972; *Jakeman and Tough*, 1988; *Plant*,

[1]Now at Applied Physics Laboratory, College of Ocean and Fishery Sciences, University of Washington, Seattle.

Paper number 93JC00862.
0148-0227/94/93JC-00862$05.00

1991] or from measurements at very low grazing angles [*Watts and Ward*, 1987].

However, many of our most important theories and applications of microwave backscatter from the sea depend heavily on the spatial and temporal correlation properties of the backscatter. Classic composite surface theories of microwave backscatter from the sea depend on rapid spatial decorrelation of the return so that signals from elementary "facets" of indeterminate size may be added incoherently [*Wright*, 1968; *Bass et al.*, 1968]. Prevailing theories of synthetic aperture radar (SAR) imagery of the ocean assume rapid spatial decorrelation of the backscatter on scales of the SAR resolution [*Alpers and Rufenach*, 1979; *Plant and Keller*, 1983; *Hasselmann et al.*, 1985; *Lyzenga*, 1988; *Kasilingam and Shemdin*, 1988]. These theories also require a knowledge of the correlation time or, equivalently, the velocity spread over resolution cells and integration times in order to predict the image accurately. Furthermore, predictions of signal-to-clutter ratios for SAR imagery require a knowledge of the variability of the cross section on scales of resolution cells and integration times [*Alpers and Hasselmann*, 1982]. Finally, the ultimate limit on the accuracy to which the wind vector over the ocean may be measured by scatterometry is determined by the normalized variance of the backscatter, which at aircraft altitudes and below is not well known [*Fischer*, 1972; *Jakeman and Tough*, 1988; *Plant*, 1991].

In this paper we report measurements that attempt to provide quantitative estimates of these important parameters of backscatter from the sea for a variety of illuminated areas. We have varied the illuminated areas for both X and Ka band microwave systems over more than a factor of 10 while maintaining a constant incidence angle of 45°. These measurements allow us to observe the area dependence of the normalized radar cross section, σ_0, of the sea, its variance, and the Doppler bandwidths. By fitting these measurements to theory [*Plant*, 1991], we are able to deduce correlation areas and hence upper limits on correlation lengths along with velocity spreads and correlation times, both of which depend on illuminated area. In the next section we describe our experimental techniques. In section 3 we present the measurements of σ_0, which indicate that the normalized cross section of the sea does not depend on illuminated area. In section 4 we compare the area dependence of the normalized variance of σ_0, that is, the variance divided by the square of σ_0, with theory. In doing so, we obtain estimates of the parameters of the theory, namely, correlation areas and normalized variances of elementary facets. In section 5 we compare velocity spreads derived from Doppler bandwidths with theory and estimate correlation times for various illuminated areas. Finally, section 6 summarizes our results and draws inferences for SAR imagery of the ocean.

2. Experimental Procedures

The experiments were performed in November 1990 on the German Research Platform Nordsee (FPN) as part of the SAR and X Band Ocean Nonlinearities (SAXON)-FPN experiment. Figure 1 shows the location of this tower in the North Sea. A retractable elevator was built for us by Reedereigemeinschaf Forschungsschiffahrt, the German company that operates the tower, and was mounted on the north side of the platform. Figure 2 is a drawing of the tower showing the location of the elevator. The two microwave systems were continuous-wave, dual-polarized systems similar in design to those we have used previously. Figure 3 gives a

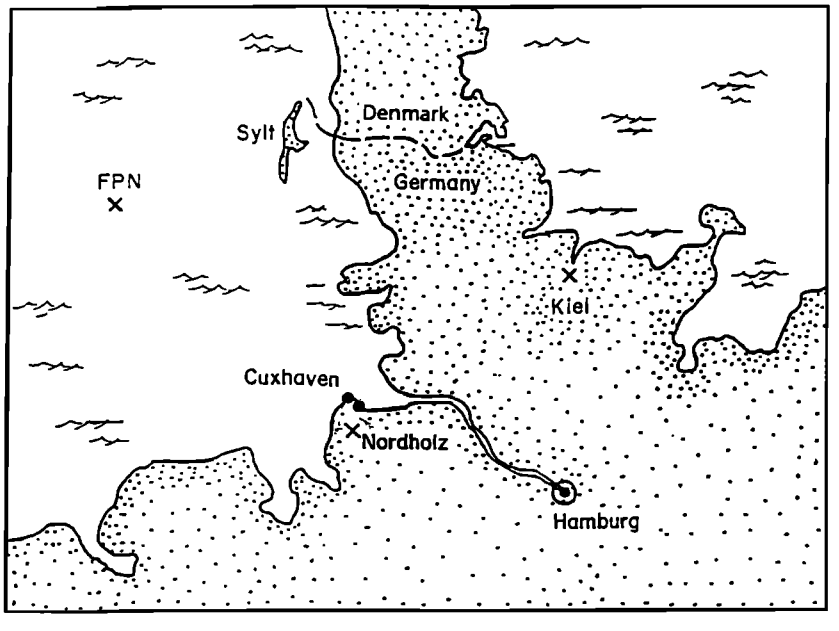

Figure 1. Location of Forschungsplattform Nordsee (FPN) in the North Sea.

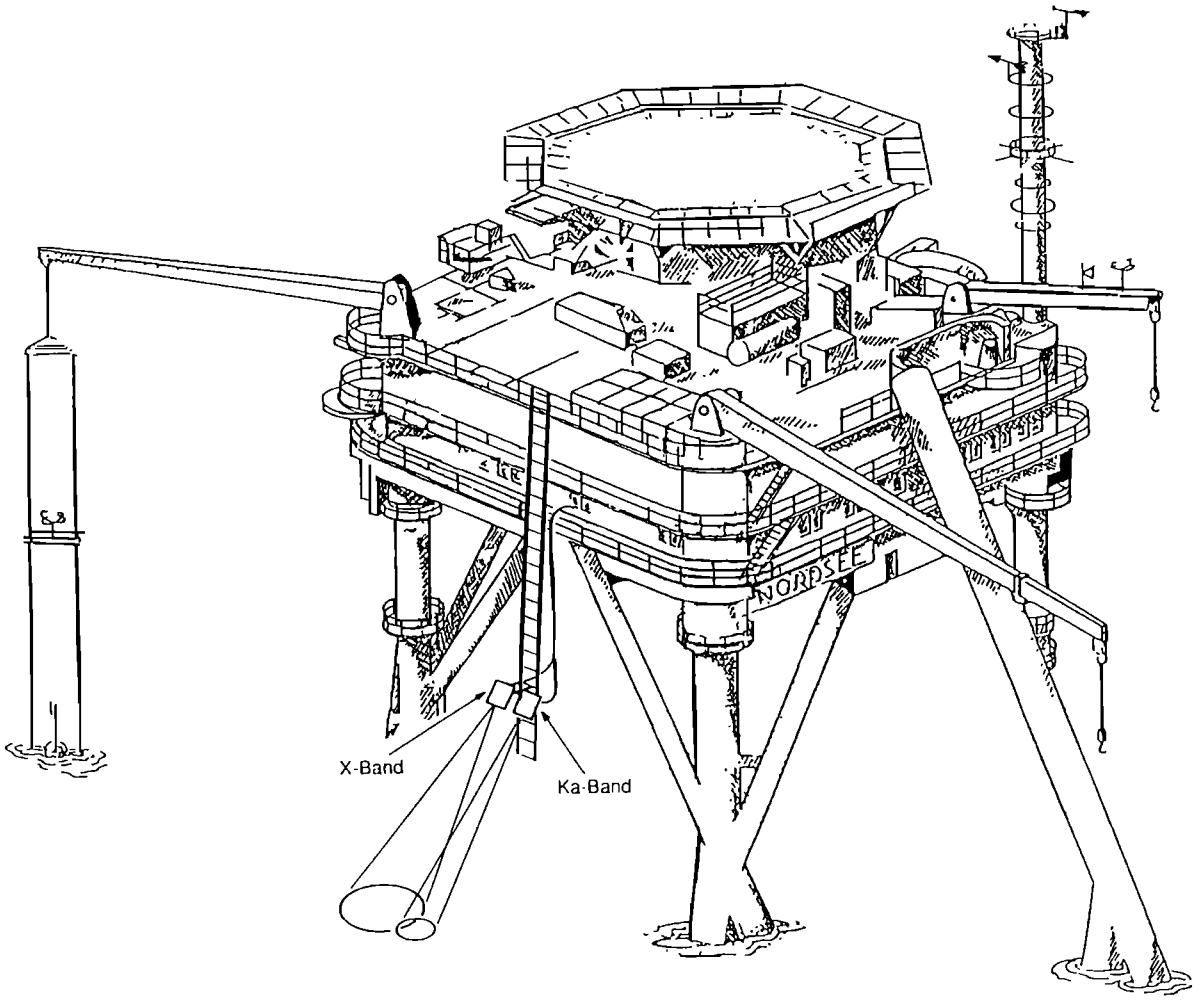

Figure 2. Drawing of FPN showing the location of the elevator on the north side of the platform.

block diagram applicable to both systems while Table 1 gives their specifications as deployed in this experiment. For the data presented in this paper the microwave antennas were always pointed toward north and were operated primarily at a 45° incidence angle. A few hours of data were collected at a 20° incidence angle but are not presented here owing to uncertainties about tower effects on the data, especially at low antenna heights. In order to minimize these tower effects on the data that are presented, only data collected with wind directions within 45° of north will be shown except for two 10° calibration runs discussed below. This restriction caused us to discard more than 75% of the data collected.

We were careful to operate in the far field of the antennas. Antenna heights varied from 7.5 to 27 m. Thus for the 45° incidence angle the minimum range to the illuminated spot was 10.6 m while for the antenna diameters and wavelengths shown in Table 1, the far fields of the antennas are 2.4 m for X band and 5.6 m for Ka band. The separation between the two antennas of each system was about 20 cm, which yielded sufficient beam overlap at all antenna heights so that the change in two-way beam width with antenna height was negligible. Thus the illuminated area was given by

$$A = \frac{\Phi_v \Phi_h h^2}{\cos^3 \theta_i} \tag{1}$$

where Φ_v and Φ_h are two-way, half-power, full vertical and horizontal beamwidths, h is antenna height, and θ_i is incidence angle [*Plant*, 1990]. The microwave systems were calibrated both before and after the experiment. This was accomplished by measuring system output voltages for returns from corner reflectors of known cross section, σ_c, at various ranges, R_c. The sum of the squares of the I and Q outputs divided by the square of the dc reference voltage shown in Figure 3 theoretically produces a constant for a given corner reflector at a fixed range. If we let this ratio be ρ_c for the corner reflectors and ρ for ocean measurement conditions, then it is easy to show from the radar equation that the normalized radar cross section of the ocean is given by

$$\sigma_0 = \frac{C \rho R^4}{A} \tag{2}$$

where R is the range to the ocean surface and the calibration constant C is given by

$$C = \frac{\sigma_c}{\rho_c R_c^4} \tag{3}$$

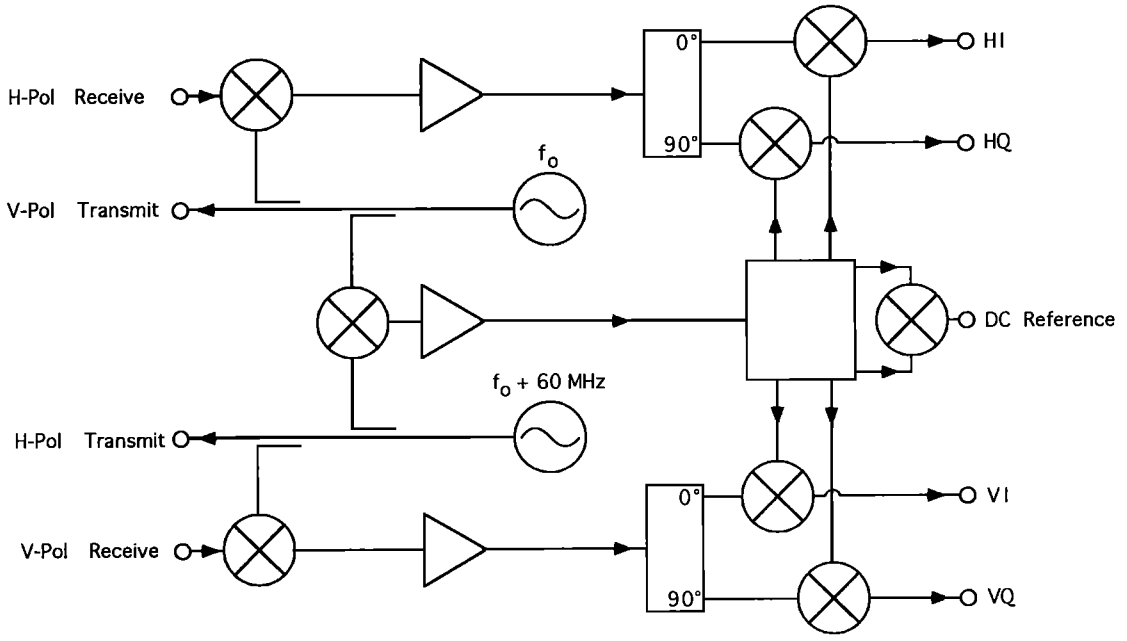

Figure 3. Block diagram of the continuous wave microwave systems.

Values of C were determined many times both before and after the experiment. Measured values varied a bit as expected, but the standard deviation of the mean was always less than 6%. Thus we believe that our cross sections have 95% confidence intervals of about ±12%. As a check of our absolute calibration levels, we took some data with the techniques outlined below at a 10° incidence angle. These values are given in Table 2. Most theories and experiments indicate that at X or Ka band these values should lie within the range of 6.5 to 8.5 dB over a broad range of wind speeds. Table 2 indicates that our X band results do indeed fall within this range but the Ka band values seem to be a bit larger.

Data from the microwave systems were fed into a 16-channel sample-and-hold unit whose output was analog-to-digitally converted at a rate near either 2 or 3 kHz. The sample-and-hold unit was used to ensure that all data channels were sampled precisely simultaneously. The rise time of the sample-and-hold circuitry was 10 μs so that each sample was obtained essentially instantaneously. An IBM compatible 386 computer was used to process and store the digital data. Each microwave system fed five channels to this computer. These channels consisted of in-phase and quadrature information for both HH and VV polarizations along with the reference voltage that monitored system gains. Although we stored some of these raw data directly on WORM optical disks, all data to be discussed below were preprocessed prior to being stored on these disks.

For each microwave system and polarization the following preprocessing was performed: A sample set consisting of 512 samples was obtained, and an instantaneous, uncalibrated σ_0 value was computed by squaring the I and Q channels and adding them. The mean and variance of these 512 squared values were computed. The raw I and Q channels were also fast Fourier transformed on a digital signal processing board, and the first and second moments, f_1 and f_2, of the Doppler spectrum were computed as follows:

Table 1. Specifications of the Microwave Systems

	X Band	Ka Band
Frequency, GHz	10.0	35.0
Wavelength, cm	3.0	0.86
Polarization	HH, VV	HH, VV
Type	coherent, CW	coherent, CW
Transmitted power, mW	100	20
Antenna diameter, cm	19.0	15.5
E-plane one-way half-power beamwidth, deg	10	4.3
H-plane one-way half-power beamwidth, deg	13	4.4
Linear dynamic range, dB	70	70

Table 2. Measured σ_0 at a 10° Incidence Angle

Height, m	Wind Speed, m s^{-1}	Wind Direction, deg	Ka HH, dB	Ka VV, dB	X HH, dB	X VV, dB
22.8	11.9	110	8.7	8.9	7.4	7.4
22.6	9.6	120	9.1	9.3	7.6	7.4

$$f_1 = \int_{-f_n}^{f_n} fS(f)df \Big/ \int_{-f_n}^{f_n} S(f)df \qquad (4)$$

$$f_2 = \int_{-f_n}^{f_n} (f - f_1)^2 S(f)df \Big/ \int_{-f_n}^{f_n} S(f)df \qquad (5)$$

where $S(f)$ is the Doppler spectrum obtained by taking the magnitude squared of the sum of the I and Q Fourier transforms and f_n is the Nyquist frequency. The resulting values of f_1 and f_2 for the two polarizations were stored on optical disk along with the mean and variance of σ_0 for each polarization and the average of 512 values of the reference channel. Thus for each microwave system, nine values were stored on disk every $512/2000 = 0.26$ s or $512/3012 = 0.17$ s, depending upon the initial sampling rate. We will refer to the values that were actually stored on disk as the secondary samples.

Subsequent to the field experiment, the data were transferred from optical disks to a Sun SPARCstation for further processing. Floppy disks containing environmental data were obtained from other investigators and put into output files along with the final, processed microwave data to be described below. For the analysis presented below, we used primarily 10-minute-averaged wind speeds and directions measured at 46 and 47 m above the mean water level. When these were not available, we substituted hourly readings from the tower log. This occurred about 20% of the time. We do not use friction velocities in this work owing to the small number of values that were obtained for favorable wind directions during SAXON-FPN.

From the data recorded during the field experiment, calibrated values of σ_0 were computed using (1)–(3) applied to each secondary sample. The elevator bent a few degrees when the microwave systems were at their lowest level, so we corrected the incidence angles for this distortion as follows:

$$\theta_i = \theta_0 - 9.8 + 0.77h_0 + 0.015h_0^2 \qquad (6)$$

where θ_0 is the nominal incidence angle in degrees and h_0 is the height of the antenna above the mean low water level. In order to get h_0 for use in (1), we corrected the height above mean low water level for tidal variations. Values of σ_0 reported below have been corrected to those at a nominal incidence angle of 45° by subtracting 0.3 dB for each 1° difference between the actual incidence angle and 45°. From (6) we see that the maximum correction is −1.2 dB. The σ_0 values obtained for each secondary sample were averaged, as antilogs, over a set of 4096 values. These averaged values, which we will call the final samples, are displayed in section 3. Table 3 summarizes the various sampling rates and integration times used in this study. The entire data set collected during SAXON-FPN consisted of 1790 final sample sets.

Table 3. Different Levels of Sampling Used in This Study

	Initial Samples	Secondary Samples	Final Samples
Sample rate or period	2000 Hz or 3012 Hz	0.170 s or 0.255 s	irregular
Integration time	10 μs	0.170 s or 0.255 s	696 s or 1045 s

Final samples of variances were computed from the mean of recorded secondary samples by adding the variances of the secondary samples of σ_0. From these, final samples of the normalized variance, n, were computed by dividing by the square of the final samples of σ_0 without the correction for the variable incidence angle. Thus if subscripts i, s, and f refer to initial, secondary, and final samples, we have

$$n = \frac{\overline{\text{var}_s\{\sigma_{oi}\}} + \text{var}_f\{\sigma_{os}\}}{\sigma_{of}^2} \qquad (7)$$

The result, n, is the normalized variance of the initial samples of σ_0 over the final integration time. Thus it corresponds to the normalized variance computed from a set of 512 × 4096 initial samples of σ_0.

The particular values obtained for the first moment of the Doppler spectrum, f_1, depend on surface currents and antenna look directions; they are of interest in this study only through their involvement in the computation of second moments, f_2. Thus we will pursue them no further. Final samples of f_2 were computed by simply averaging 4096 secondary samples together. Data will be displayed below, however, in terms of radial velocity spreads computed from the following equation:

$$\delta v_r = \frac{\lambda(\overline{f_2})^{1/2}}{2} \qquad (8)$$

where λ is microwavelength.

3. Normalized Radar Cross Sections

Final samples of σ_0 were binned according to the wind speed and illuminated areas at which they were taken. Plots of the resulting values versus illuminated area are shown for various wind speeds in Figure 4 for X band and Figure 5 for Ka band. These results indicate that, while a high degree of variability exists within any wind speed range, no dependence on illuminated area can be discerned in the graphs.

We have taken some care in computing error bars in these two figures and believe them to be conservative estimates of our overall experimental error. Below we will show that the maximum values of normalized variance that we observed were about 12 for X band and 40 for Ka band. Initial samples of the cross section were obtained at time intervals less than the correlation time, so they are not all independent. We will also show below that the largest correlation times, t_o, we obtained were 14 ms for X band and 6 ms for Ka band. A conservative estimate of the number of independent initial samples averaged to get a final sample is $512 \times 4096/(3012t_o)$. This really assumes that decorrelation implies statistical independence, which is not strictly true, but the difference, which represents large-scale organized correlation of the cross section, is small. Thus we estimate that the ratio of the standard deviation of the mean to the mean for the final samples is about 0.015 for X band and 0.05 for Ka band. This is the uncertainty induced by the inherent variability of ocean backscatter. If we square these values and add the variance we found in calibration, then twice the square root of the result is the 95% confidence half interval, assuming that a large enough number of independent initial samples have been averaged to get a final sample that obeys Gaussian statistics. This number is about ±0.5 dB for X band and ±0.7 dB for Ka band.

Figures 4 and 5 clearly show that the final samples of σ_0 vary well beyond these 95% confidence intervals. This indicates that the geophysical processes responsible for backscatter change their statistical properties on scales long compared to the 11 or 17 min intervals represented by the final samples. Such geophysical variability of the cross section should be correlated with geophysical variables with similar timescales, but we have not been able to isolate these variables in this study.

We did not feel that the wind data available in large quantities in this study were sufficiently relevant to processes at the surface to warrant a detailed investigation of the wind dependence of σ_0. We did, however, check to see if differences existed in the wind speed dependence of X and Ka band cross sections. Since these were obtained simultaneously, such differences should be obvious even if the actual surface wind speed is somewhat inaccurate. Figure 6 shows the ratio of X and Ka band cross sections as a function of wind speed. Obviously, the dependence is remarkably similar. On a Bragg scattering/composite surface model, this indicates that short wind-generated waves with wavelengths of 0.6 cm and 2.1 cm respond to the wind in a very similar manner. The value of this constant ratio may not be an actual difference in cross section but, rather, indica-

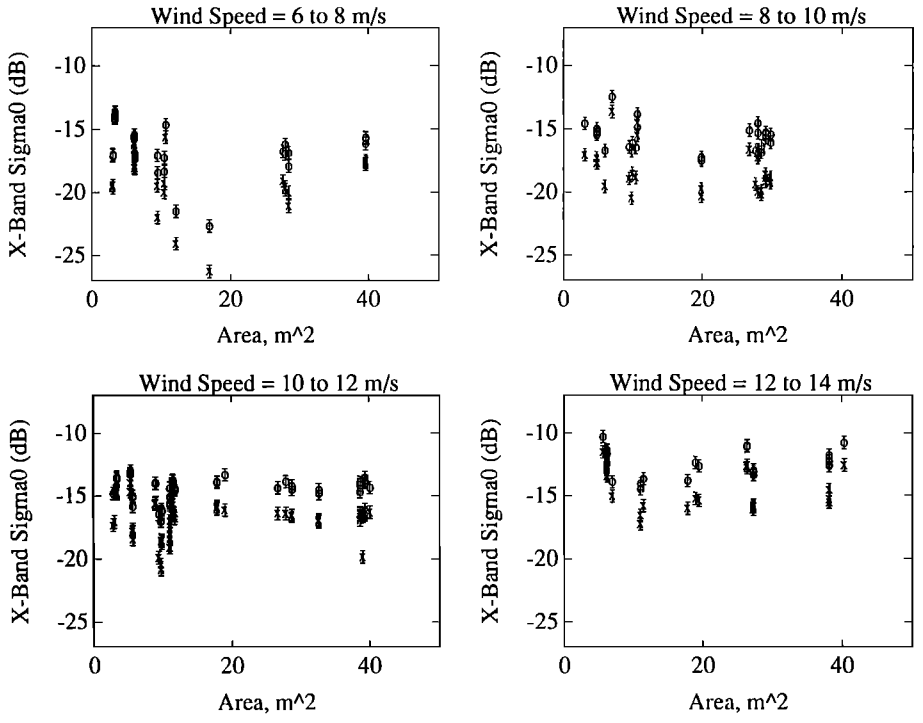

Figure 4. X band normalized radar cross sections of the sea, σ_0, versus illuminated area. Data are shown for four different ranges of wind speed. Open circles represent VV polarization; Xs represent HH polarization. Error bars indicate 95% confidence intervals for the measured values.

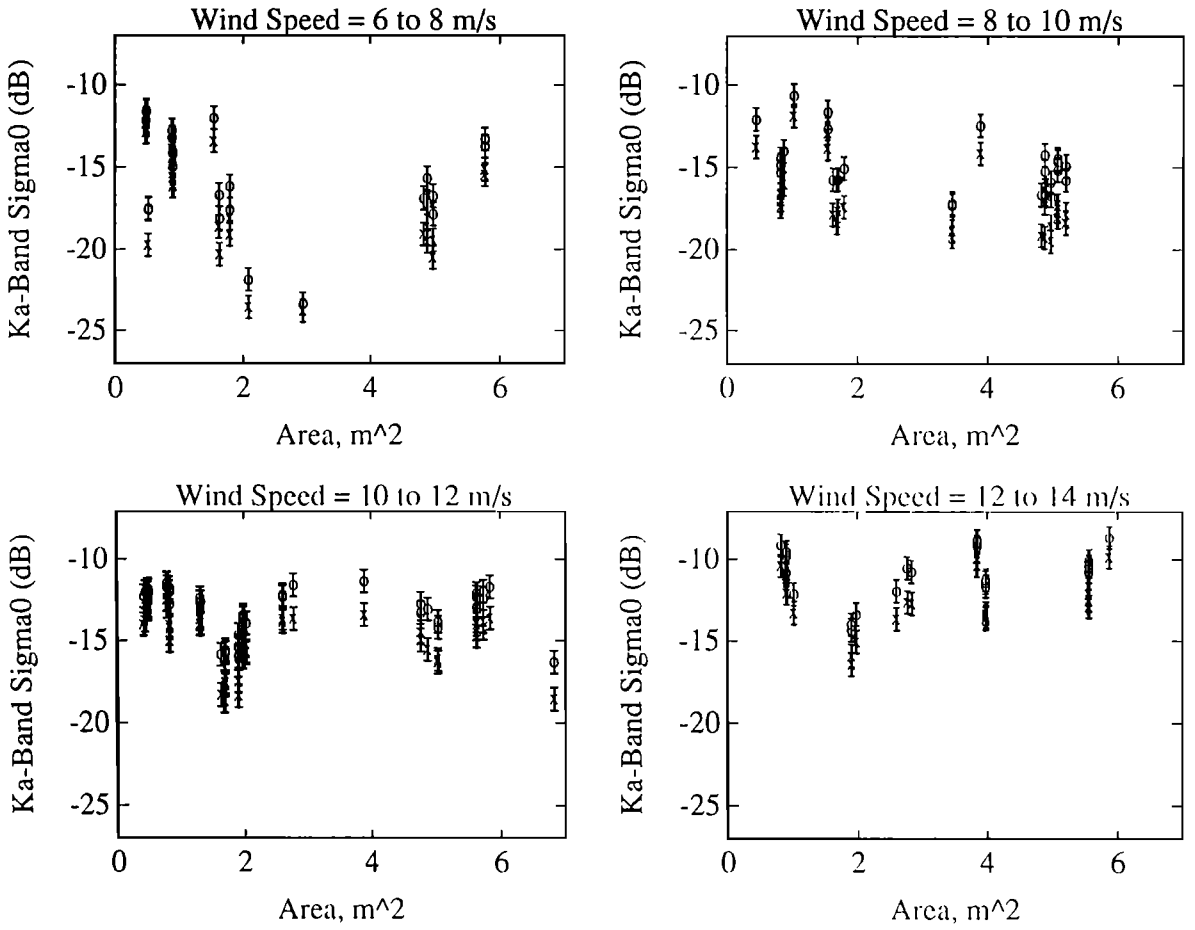

Figure 5. Same as Figure 4 but for Ka band.

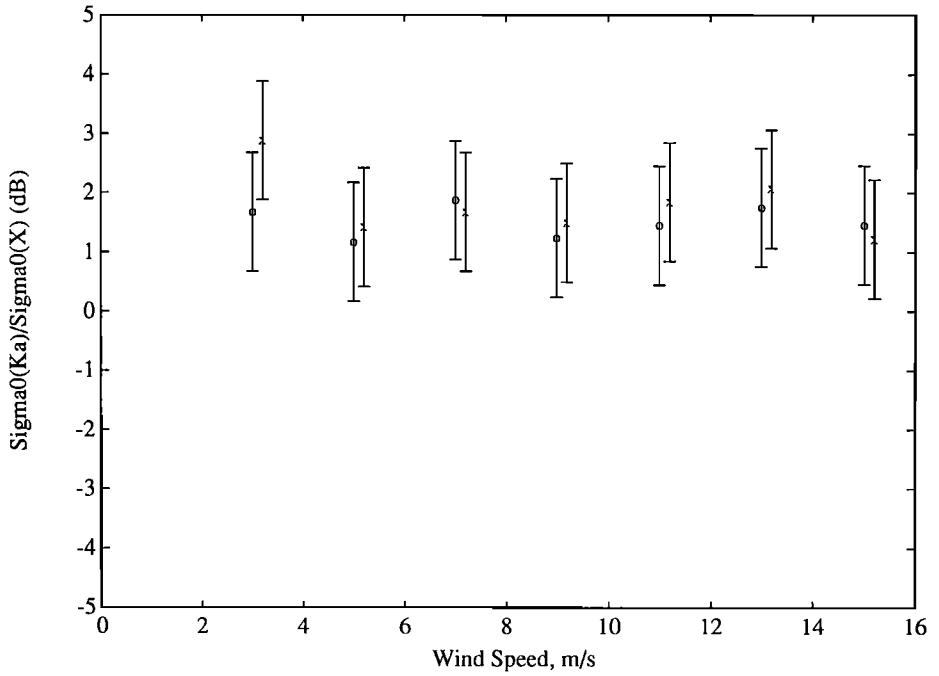

Figure 6. Ratio of normalized radar cross sections at Ka and X bands plotted versus wind speed. Open circles represent VV polarization; Xs represent HH polarization. Error bars are 95% confidence intervals.

tive of problems in our absolute calibrations, probably at Ka band. The offset shown in Figure 6 is very similar to that shown for 10° incidence angles in Table 2.

4. Normalized Variances, Correlation Areas, and Facet Variances

Final samples of the normalized variance of microwave backscatter from the sea, n, are shown in Figure 7 for X and Ka bands and for both polarizations. The wind speed range in this figure, 0–20 m s^{-1}, includes all wind speeds encountered during the experiment; except for the wind direction, no other environmental variables have been restricted in Figure 7. Figures 8 and 9 show the same type of plots for more restricted ranges of wind speeds, 4–6 m s^{-1} in Figure 8 and 10–12 m s^{-1} in Figure 9. We were not able to restrict the range of wind speeds more than this or to investigate other 2 m s^{-1} ranges owing to the low number of data points that satisfied such requirements. Note that all the figures indicate that n decreases with increasing illuminated area, that Ka band is more variable than X band, that HH polarization is more variable than VV, and that n does not drop much below 2 for the largest areas illuminated in this experiment.

The solid lines in Figures 7, 8, and 9 represent the best fit of the theory of *Plant* [1991] to the data. According to this theory, n can be expressed in terms of fundamental scattering parameters and surface wave slope as follows:

$$n = \frac{t_o}{\sqrt{T^2+t_o^2}} \left\{ 1 + \frac{a_o}{2A'+a_o} \times \left[n_o - 1 - \int |m(\vec{K},\Omega)|^2 S(\vec{K},\Omega) d\vec{K} d\Omega \right] + \int |m(\vec{K},\Omega)|^2 S(\vec{K},\Omega) \exp\left(-\frac{K^2 A'}{\pi}\right) d\vec{K} d\Omega \right\} + \int |m(\vec{K},\Omega)|^2 S(\vec{K},\Omega) \exp\left(-\frac{K^2 A'}{\pi} - \frac{\Omega^2 T^2}{4\pi}\right) d\vec{K} d\Omega \quad (9)$$

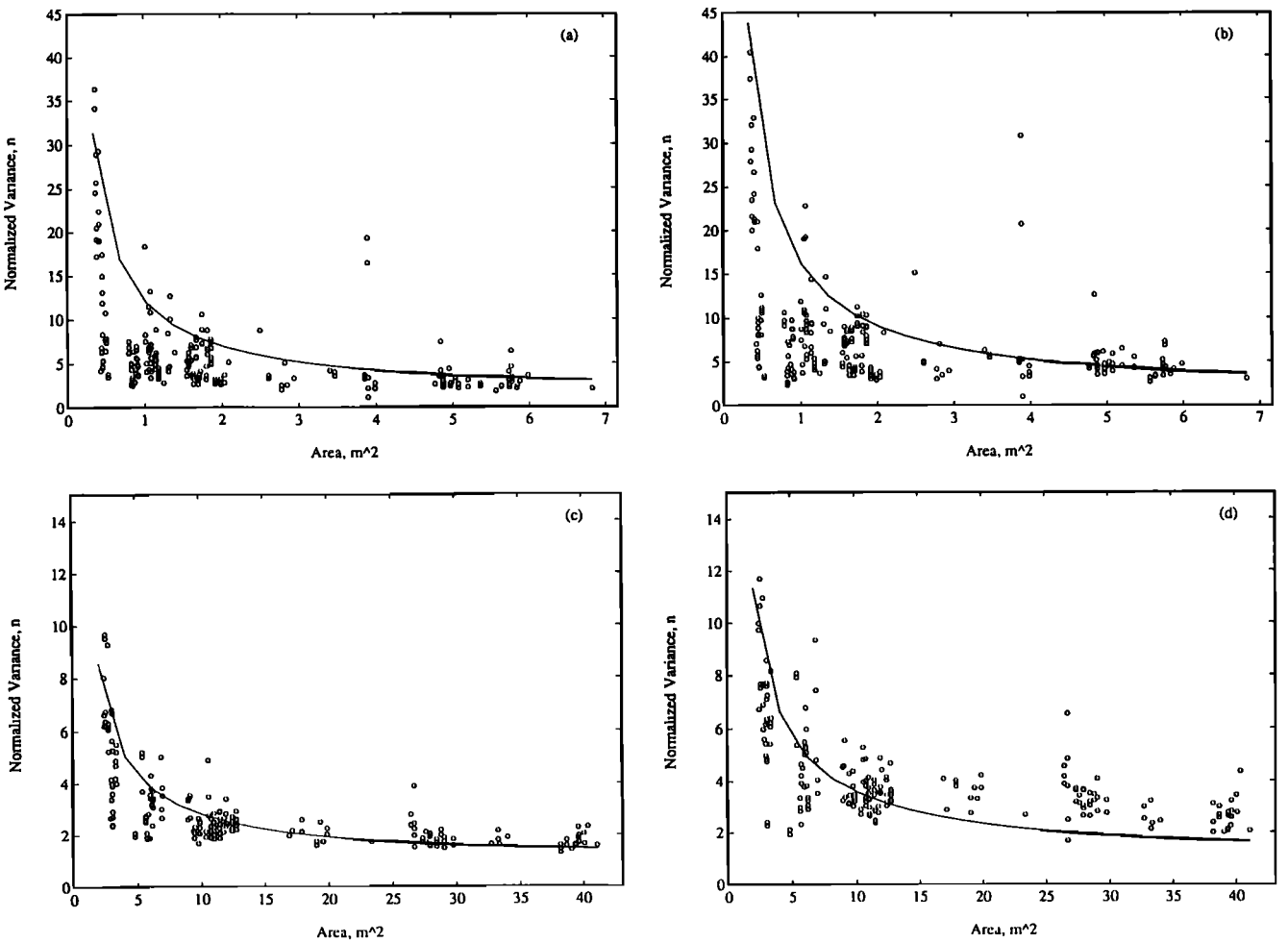

Figure 7. Final samples of normalized variance, n, versus illuminated area. Open circles indicate data while the solid line is the best fit of the theory of *Plant* [1991] to these data. Wind speeds are 0 to 20 m s^{-1} and wind direction is within 45° of north, the antenna look direction; all other environmental parameters are unrestricted. (a) Ka band, VV polarization, (b) Ka band, HH polarization, (c) X band, VV polarization, (d) X band, HH polarization.

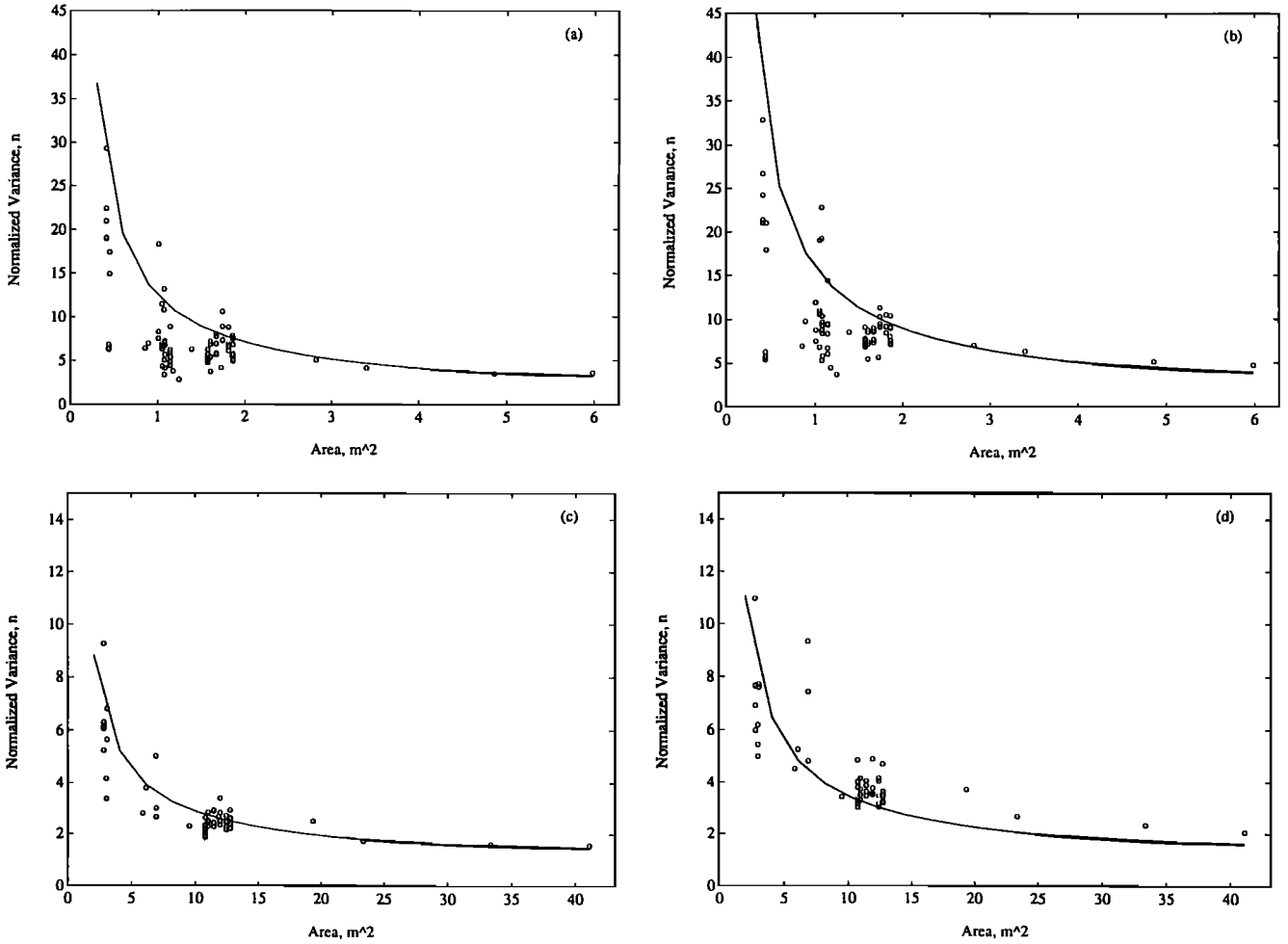

Figure 8. Same as Figure 7, except for a wind speed range of 4–6 m s^{-1}.

where

$$A' = \frac{A(A + a_o)}{2A + a_o} \tag{10}$$

Here, t_o and a_o are correlation times and areas for the received power, n_o is the normalized variance of a single facet, m is the modulation transfer function relating fluctuations in received power to surface wave slope, S is the spectrum of these surface wave slopes, K is wavenumber, and Ω is radian frequency.

The integration time, T, for the initial samples was 10 μs as given in Table 3, while typical correlation times given in the following section are on the order of several milliseconds and relevant wave periods are, of course, much longer. Thus all factors involving T in the above expression were set to one, that is, $T = 0$, in comparing the theory with the data collected here. In order to evaluate (9) and (10), we assumed a dispersion relationship, $\Omega^2 = gK$, where g is acceleration due to gravity, to be valid down to 4 m, the shortest wave over which the integrals in (9) were taken. This allowed the integral over K to be carried out trivially. $S(f)$, where $\Omega = 2\pi f$, was then determined from the measured buoy wave height spectra by multiplying them by K^2. The modulation transfer function, m, which is necessary to evaluate (9) was measured during SAXON-FPN using the same X and Ka band systems used here. Methods and results of these measurements are the subject of a separate paper [*Plant et al.*, this issue]. It is straightforward to show that $|m(f)|^2 S(f)$, where $m(f)$ is the measured modulation transfer function is precisely the result of the angular integration implied in (9) [*Plant*, 1989]. The final integral in (9), that over Ω, was then converted to an integral over f and carried out numerically.

Thus all that remained in order to evaluate (9) were proper values for a_o and n_o. Since these were unknown, we stepped through 20 values of a_o and 40 values of n_o to produce 800 theoretical estimates of n to compare with each measured one. The files containing the final samples were searched in order to find all measurement conditions that fit the specified restrictions on wind speed, direction, incidence angle, microwave frequency, and polarization. Linear fits of the resulting data points to theoretical estimates with given values of a_o and n_o were then produced. We found that the slope of the best fit line was closest to one when a relationship existed between a_o and n_o. This relationship is given in Table 4 for the various wind speed ranges, microwave

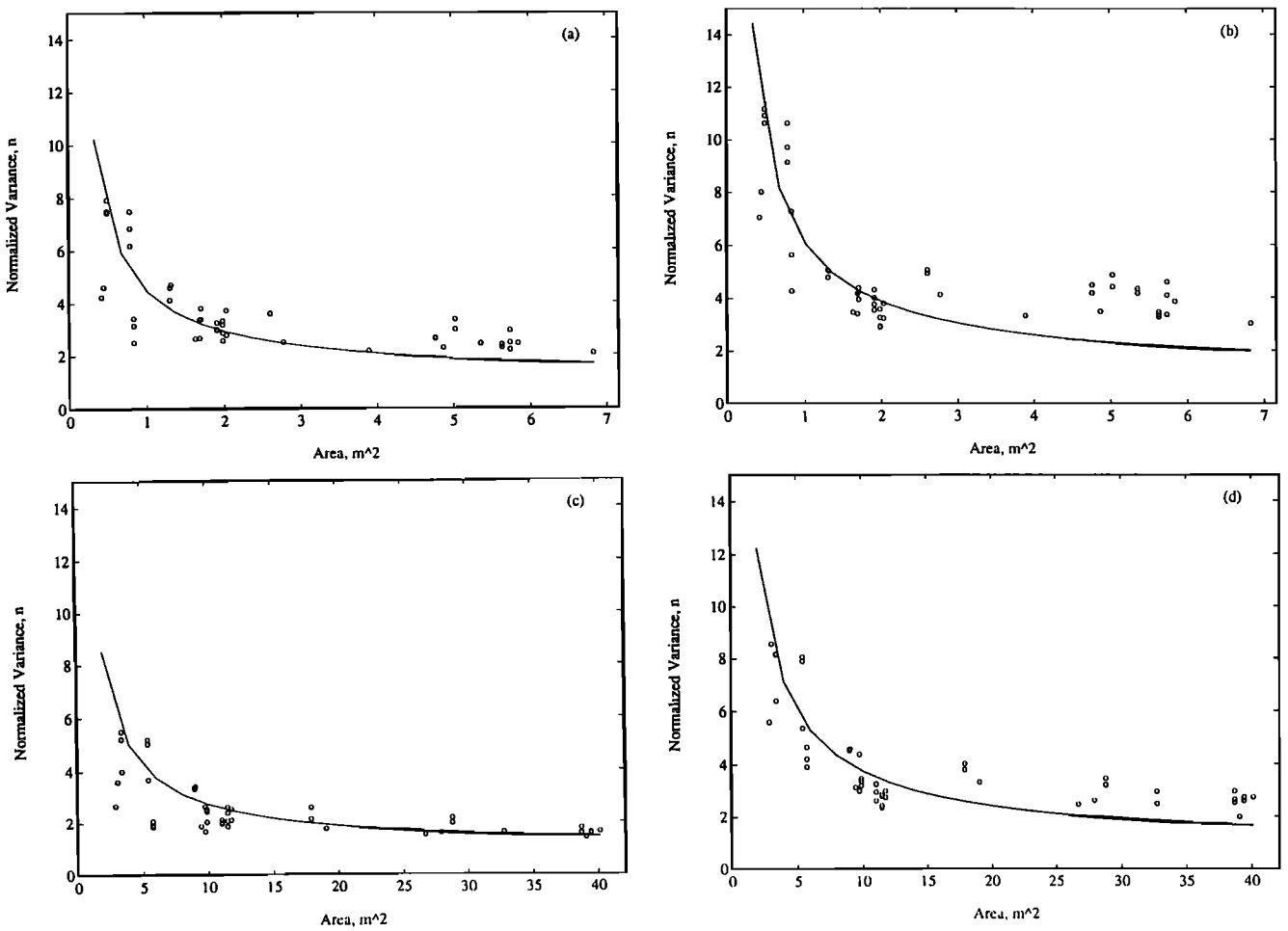

Figure 9. Same as Figure 7, except for a wind speed range of 10–12 m s^{-1}.

frequencies, and polarizations examined. Within the set of 20 values that satisfied this relationship, we examined the y intercepts of the fits, that is, the bias between theory and experiment. Figure 10 shows the results of such bias versus correlation area studies. The plots are presented with the abscissa being the number of microwavelengths contained in each dimension of a square the size of the correlation area. The discontinuities in the Ka band curves result from the finite steps used in varying a_o and n_o. The striking feature of these curves is their tendency to minimize at small values of correlation area. Although Figure 10 presents

Table 4. Best Fit Parameters for Variance Theory

Wind Speed, m s^{-1}	Band	Polarization	$n_o * a_o$, m^2	a_o, cm^2	$(a_o/\lambda)^{1/2}$	n_o	Correlation Coefficient
0–20	Ka	V	$51a_o + 9.8$	2.9–18.1	2–5	5500–33800	0.65
	Ka	H	$66a_o + 14.0$	2.9–11.8	2–4	12000–48000	0.64
	X	V	$12a_o + 14.6$	44–576	4–8	265–3330	0.84
	X	H	$16a_o + 19.3$	576–1296	8–12	165–351	0.77
4–6	Ka	V	$58a_o + 10.4$	11.8–47.0	4–8	2270–8870	0.74
	Ka	H	$64a_o + 13.4$	2.9–26.5	2–6	5120-46300	0.67
	X	V	$12a_o + 14.5$	324–900	6–10	173–460	0.87
	X	H	$15a_o + 18.8$	324–900	6–10	224–595	0.82
10–12	Ka	V	$12a_o + 3.0$	73–188	10–16	172–423	0.79
	Ka	H	$15a_o + 4.3$	106–188	12–16	243–420	0.83
	X	V	$9a_o + 14.5$	144–324	4–6	456–1016	0.79
	X	H	$14a_o + 20.6$	576–1296	8–12	173–372	0.86

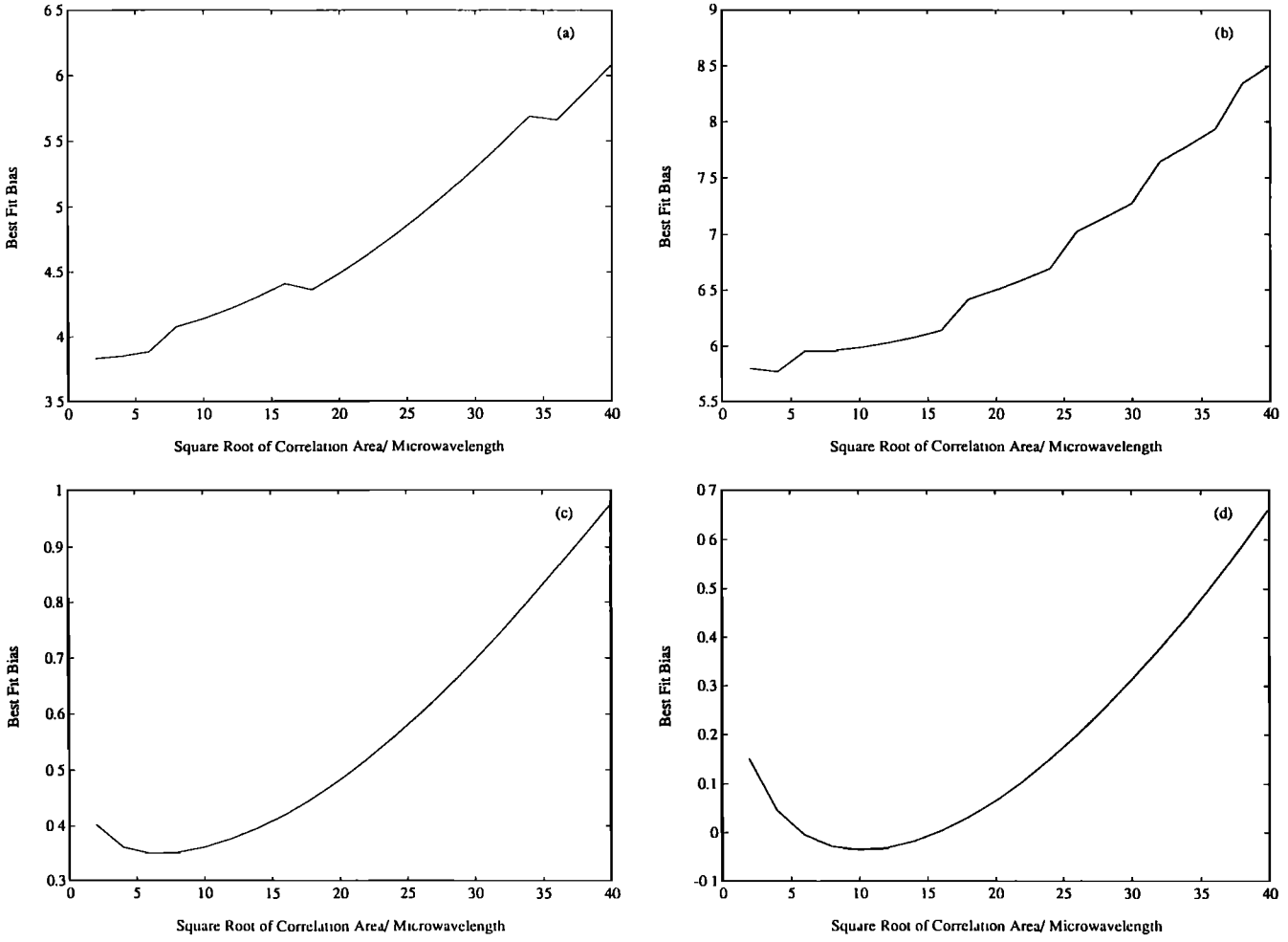

Figure 10. Bias in best fit to data for various values of $(a_o)^{1/2}/\lambda$.

only the full data set, this tendency was present in all subsets examined. In Table 4 we give the approximate values of a_o and number of microwavelengths at which these minima occurred. The theoretical curves shown in Figures 7, 8, and 9 have correlation areas in the neighborhood of these minima. Also shown in Table 4 are the range of n_o values implied by the range of a_o and correlation coefficients between the best fit set of theoretical values. The correlation coefficients varied little when the relationship between a_o and n_o was that given in Table 4.

Equation (9) shows that n should approach 1 when $A' >> a_o$ and K^2A'/π is large. The latter is the more stringent condition and, if we assume "large" to be 4, implies that A must exceed about 1000 m^2 for typical North Sea dominant wavelengths in order that $n = 1$. Since the areas illuminated in this experiment were always much smaller than this, it is not surprising that scattering fields did not achieve Gaussian statistics.

In several cases in Figures 7, 8, and 9 the theory falls significantly below the data for large illuminated areas. This may indicate that spatial correlation of received power is induced by other processes in addition to ocean surface waves. Fluctuations in surface wind speed or stress would seem to be a prime candidate. Such additional processes can be modeled simply by increasing m slightly in the low-frequency ranges. When we attempted this, the theoretical curves were indeed raised to fit the data better at high areas. Best fit correlation areas and facet variances were unchanged. The price paid was that the theoretical curves were also raised for small areas which, in some cases, appeared to degrade the fit. Overall, however, we feel that the data indicate that such additional processes probably exist.

5. Velocity Spreads and Correlation Times

Radial velocity spreads were computed both from the entire data set restricted only in wind speed and direction and from subsets taken rapidly during short periods of time. Figure 11 shows two of the latter subsets taken on November 27, 1990, under very different wind conditions. Figure 11a shows data collected between 0914 and 1424 UT when the wind speed was in the range of 10 to 13 m s^{-1} and the wind direction was between 20° and 40°. Figure 11b shows data collected between 2042 and 2354 UT when the wind speed was between

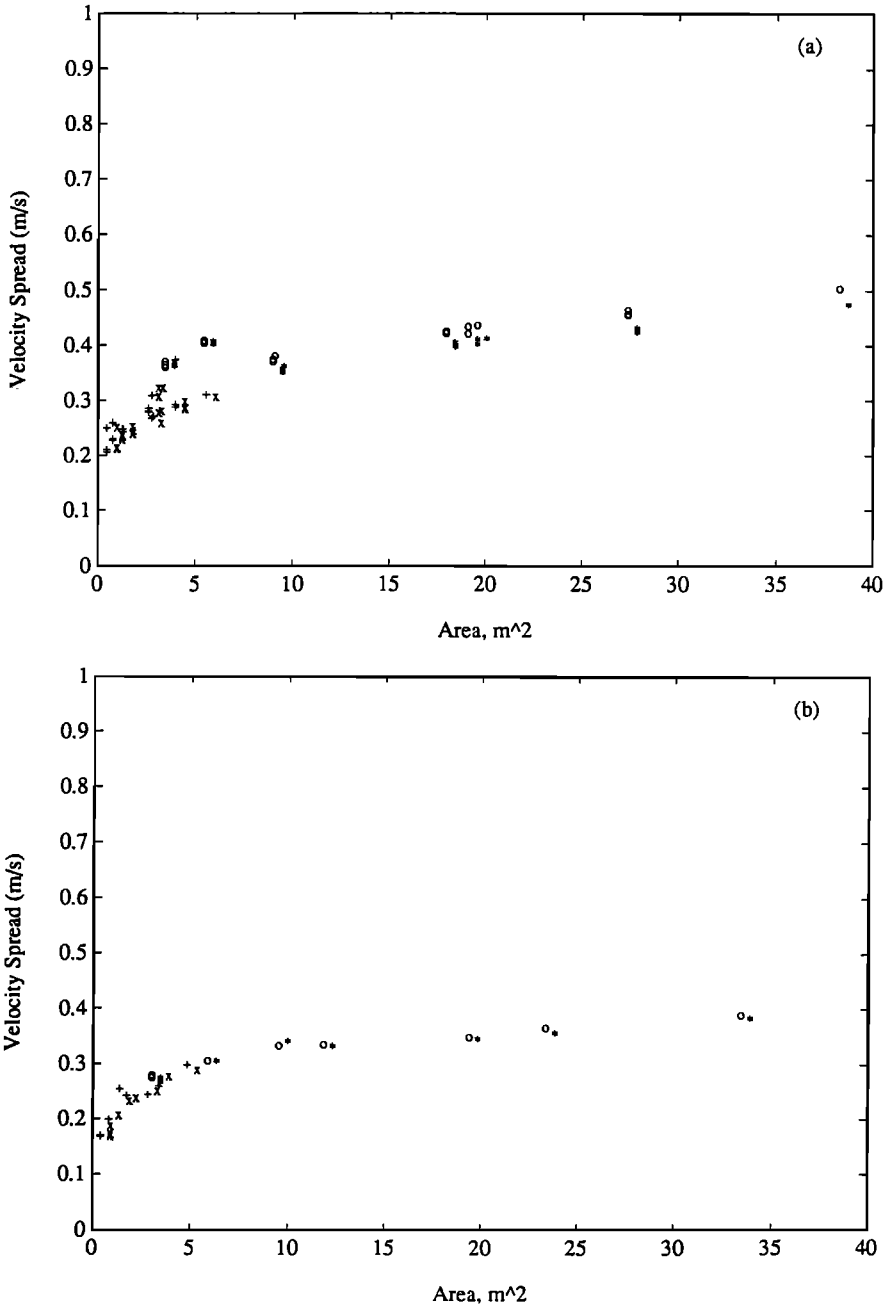

Figure 11. Radial velocity spread versus illuminated area for two data sets taken on November 27, 1990. Symbols indicate the following: plus = KaH, cross = KaV, circle = XH, star = XV. VV polarization data have been offset to the right by 0.5 m^2 for clarity. (a) 0914 to 1424 UT, wind speed 10 to 13 m s^{-1}, wind direction 20° to 40°; (b) 2042 and 2354 UT, wind speed 4–7 m s^{-1}, wind direction 20°–45°.

4 and 7 m s^{-1} and the wind direction was between 20° and 45°. Obviously, these velocity spreads are independent of polarization, and those derived from X and Ka band bandwidths agree very well with each other for the range of areas where they overlap. These features are not unexpected since all bandwidths result from the spread of surface velocities within the illuminated footprint and the data were collected simultaneously.

Figure 11 shows that radial velocity spreads depend little on wind speed; theory suggests that the dependence is really on the integral of surface wave velocity spectra. Thus we have lumped all data together in order to compare the measured values with those predicted by theory. Figure 12 shows all data collected with wind speeds between 4 and 20 m s^{-1} and wind directions within 45° of north, along with the theoretical predictions from *Plant* [1991] plotted versus the illuminated area. We did not use the very low wind speed data in this analysis since the low signal levels often made the second moment of the Doppler spectrum un-

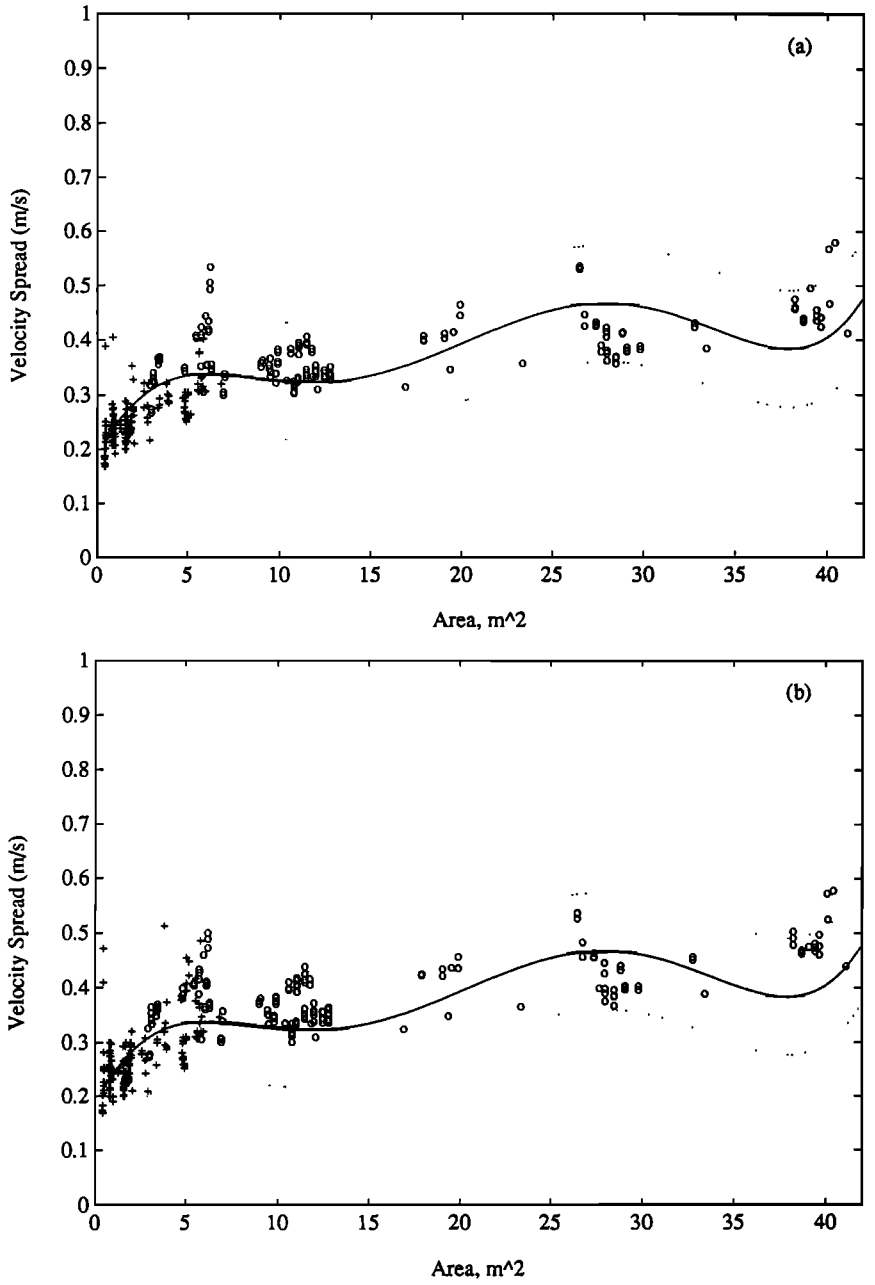

Figure 12. Velocity spread versus area for all data with wind speeds between 4 and 20 m s^{-1} and wind directions within 45° of north. The solid curve shows a fifth-order polynomial fit to the scattered theoretical values; dotted curves indicate one standard deviation. For both X and Ka band we have let $\delta v_o = 0.07$ m s^{-1}. (a) VV polarization, (b) HH polarization. Symbols are plus for Ka band, circle for X band.

reliable. Figure 12a shows results for VV polarization while Figure 12b gives them for HH polarization. The theoretical predictions are the same in both cases.

We produced the theoretical values, δv_r, by using the following equation:

$$\delta v_r = \left\{ (\delta v_o)^2 + \int G\Omega^2 F(\vec{K},\Omega)[1-\exp[-(K^2A)/2\pi] \times \exp[-(\Omega^2T^2)/4\pi)]d\vec{K}d\Omega \right\}^{1/2} \quad (11)$$

where δv_o is the intrinsic velocity spread of a facet, F is the surface wave spectrum, T is either 170 or 255 ms, and

$$G = \sin^2\theta_i \coth^2 Kd\cos^2\phi + \cos^2\theta_i \quad (12)$$

where d is water depth and ϕ is the angle between the wave propagation direction and the antenna look direction. The factor G allows for the fact that the line-of-sight value of the horizontal component of wave orbital velocity varies with wave propagation direction. This factor was incorrectly omitted by *Plant* [1991]; its value in this study was always between 0.75 and 0.9.

In order to compute the K integral in (11), we again

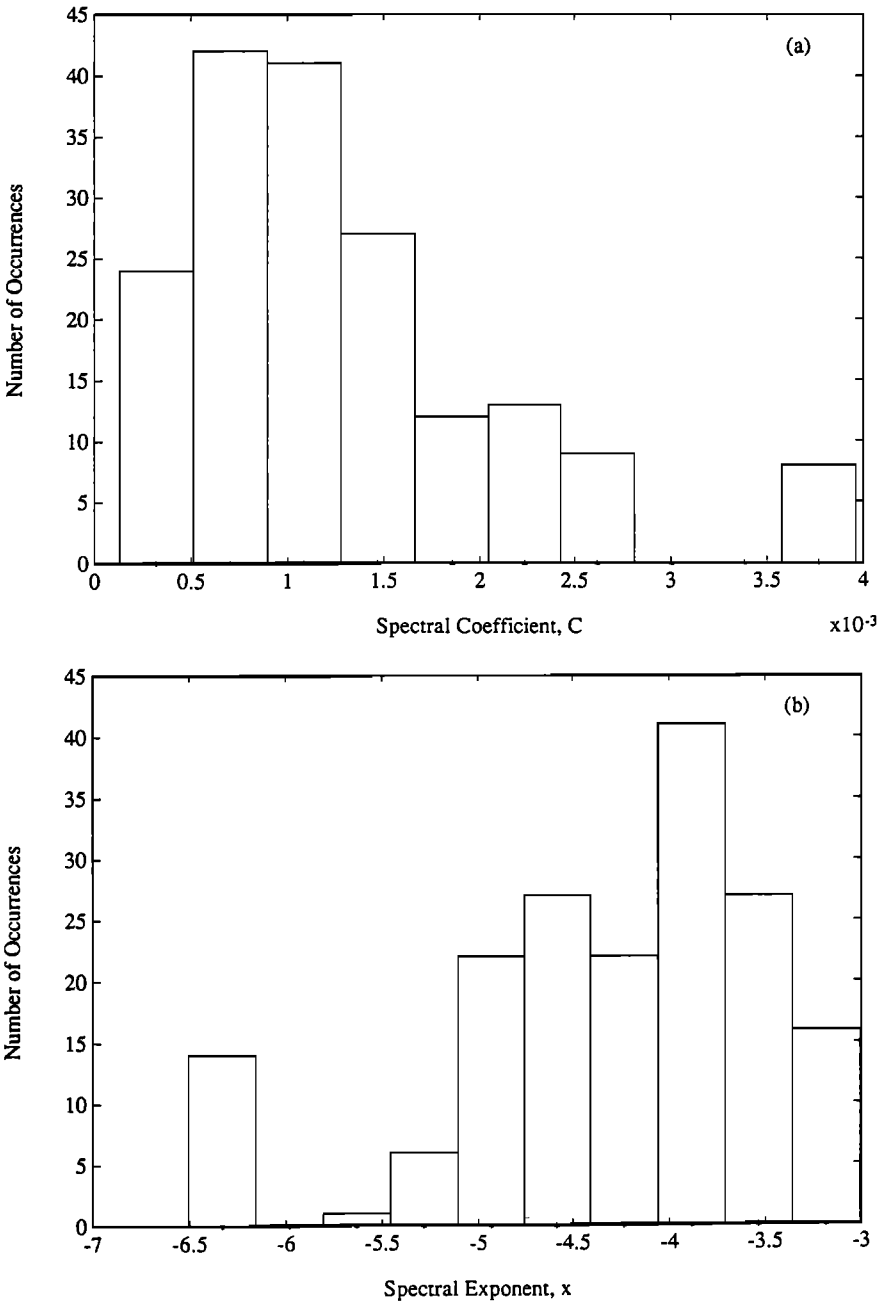

Figure 13. Parameters of the high-frequency spectral form Cf^x obtained by fitting buoy data in the frequency range 0.39 to 0.625 Hz. These values were used in the theoretical evaluations of Figure 12. (a) Histogram of spectral coefficient, C; (b) histogram of spectral exponent, x.

assumed a gravity wave dispersion relation. This is relevant only where the exponential factors in (11) differ substantially from zero; for higher frequencies it is irrelevant whether one assumes a dispersion relationship or not. Angular integrals were computed by assuming a $sech^2$ angular spreading factor after *Donelan et al.* [1985]. The widths of this factor at various frequencies were set for low frequencies by matching the rms spread from the buoy and for high frequencies by using the widths given by Donelan et al. Wave directions were set for low frequencies by using the buoy data and for high frequencies by assuming a wave direction in the wind direction. The remaining frequency integral was computed numerically after converting from Ω to f. We determined $F(f)$ from buoy data for frequencies below 40/64 Hz. We found, however, that the buoy data above about 0.4 Hz rolled off as f^{-5} to $f^{-5.5}$. Since this is faster than most studies indicate that spectra in this range should fall off [*Donelan et al.*, 1985], we corrected for rolloff caused by the finite size of the buoy by multiplying the buoy spectra by $\exp(K^2r^2/8)$ where r is the buoy radius, 1.6 m. Higher frequency omnidirectional spectra were set by fitting the resulting buoy data in the range 25/64 to 40/64 Hz to the form

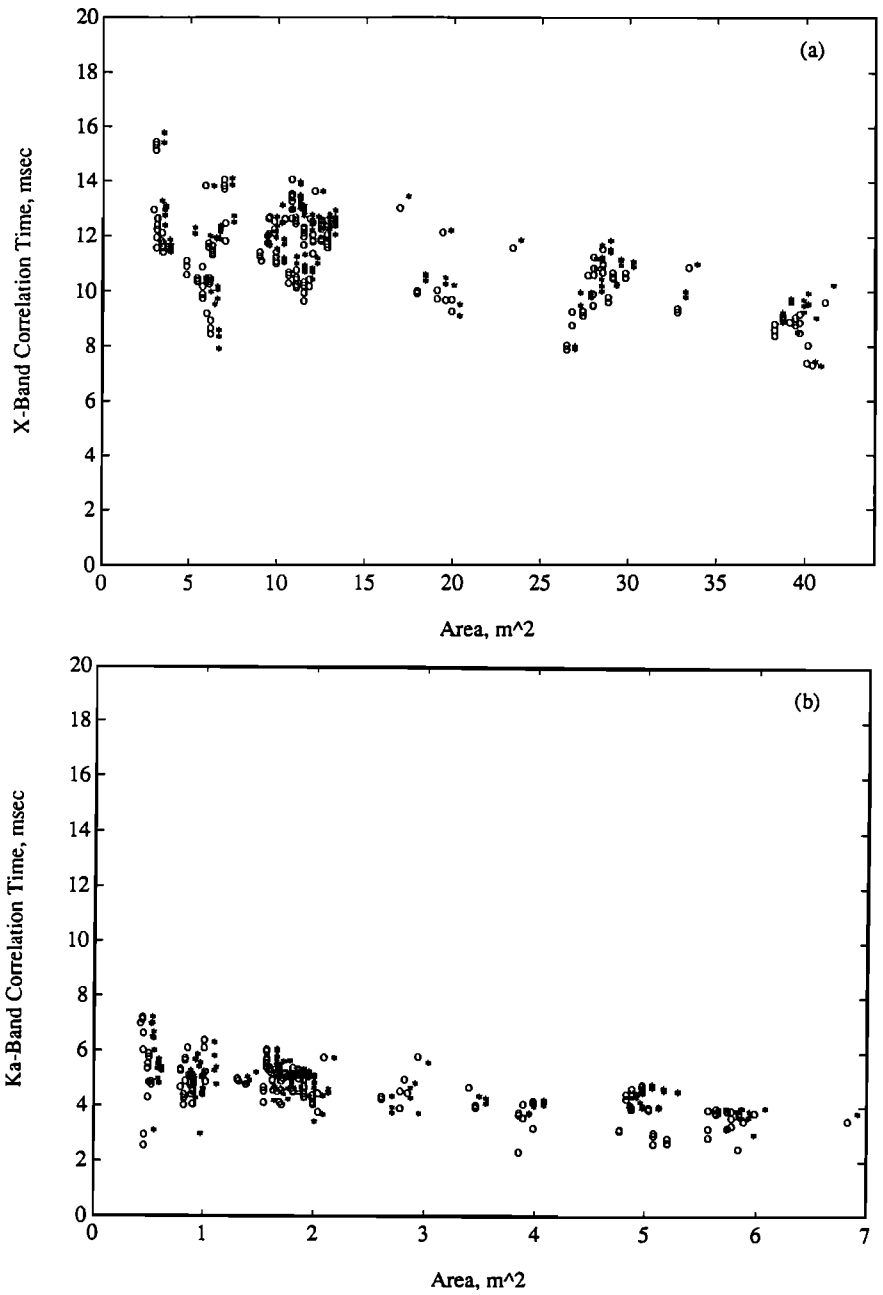

Figure 14. Correlation times versus illuminated area. Symbols indicate the following: circle, HH polarization; star, VV polarization. (a) X band, (b) Ka band. For clarity, areas for VV polarization data have been offset to the right by 0.5 m^2 for X band and 0.1 m^2 for Ka band.

$$F(f) = Cf^x \tag{13}$$

Figure 13 shows histograms of the values of C and x obtained from the entire data set. We set the upper limit of integration, f_m, to 20 Hz in evaluating (11). Given the form (13) for the high-frequency spectrum, it is easy to show that f_m is not critical. If $x = -4$ in (13), computed values would vary only about 3% for f_m ranging from 20 Hz to infinity.

Since buoy spectra were used in producing theoretical δv_r values and we had a different buoy spectrum for each data point, the theoretical values exhibit considerable scatter. Rather than confuse Figure 11 with more scattered points, we have fit a fifth-order polynomial curve to the theoretical values. This is shown as the solid curve in Figure 11. The dotted curves are at plus and minus one standard deviation of the residuals to the polynomial fit and give an indication of the scatter in the theoretical values.

As Figure 12 shows, these values produced a good fit of (11) to the data set if $\delta v_o = 0.07$ m s^{-1}. The relationship between correlation time, t_o, and velocity spread is

$$t_o = \frac{\lambda}{4\sqrt{\pi}\delta v_r} \tag{14}$$

The inferred values of t_o are shown in Figure 14 for

both X and Ka band as a function of illuminated area. Corresponding scatterer lifetimes are about 60 ms at X band and 17 ms at Ka band.

6. Summary and Inferences for SAR Imagery

For X and Ka band backscatter at 45° and both HH and VV polarization we have examined the dependence on illuminated area of the normalized radar cross section of the sea, σ_0, its variance, and the radial velocity spread inferred from the second moment of the Doppler spectrum in the case of antennas directed nearly into the wind direction. We found no evidence of a dependence of σ_0 on illuminated area or, equivalently, on antenna height. The variance of σ_0 and the velocity spread, on the other hand, do depend on illuminated area. This dependence is well characterized by the theory of *Plant* [1991]. From the fit of this theory to the data collected here, we infer that correlation lengths for both X and Ka band are on the order of 10 times the microwavelength and that the variability of backscatter from a single facet is very high; values of correlation area and facet normalized variance that gave the best fit of theory to data are given in Table 4. Velocity spreads inferred from the X and Ka band systems with their very different illuminated areas are consistent with each other. We found that a very small velocity spread due to scatterer lifetime was necessary to fit theory to data. Its exact value, however, depends on details of the high frequency part of the wave spectrum which have not been modeled exactly here.

Several interesting inferences for SAR imagery of the ocean may be drawn from these results. The assumption of spatial whiteness made in most SAR ocean imaging theories appears to be well justified, since typical SAR spatial resolution scales greatly exceed the 10 microwavelengths that we deduced for correlation lengths. Estimates of signal-to-clutter ratios for SAR imagery of the ocean and the corresponding estimates of minimum observable wavelengths have in the past used the assumption that $< \sigma_0^2 > \approx < \sigma_0 >^2$, that is, that the variance of the cross section is small [*Alpers and Hasselmann*, 1982]. The data presented here show that, in fact, for typical SAR resolution areas the variance may be quite large. Utilizing the resulting larger values for $< \sigma_0^2 >$ will substantially reduce the estimates of signal-to-clutter ratios and increase those of minimum observable wavelengths.

For azimuthally traveling waves the minimum observable wavelength is also strongly affected by the azimuthal rolloff of SAR images of the sea. In addition to velocity bunching which varies f_1, the cause of this rolloff is the width of the Doppler spectrum of the sea or, more fundamentally, the radial velocity spread over the SAR resolution cell and integration time. As shown by *Hasselmann et al.* [1985], the relevant azimuthal resolution cell size is the stationary target resolution, not the degraded resolution caused by the velocity spread itself. This is immediately obvious by the circularity involved if degraded resolution is used: the resolution determines the velocity spread which in turn determines the resolution. The process ends only when degraded resolutions are larger than the longest wave so waves would not be seen in SAR images. The measurements made here show that the theoretical expression for the velocity spread, (11), may be used to calculate the dependence of δv_r on the wave spectrum and SAR parameters if we properly allow for the fact that illuminated distances in range and azimuth may differ. For an integration time T, one must let

$$A \rightarrow \left[\left(\frac{c\tau_p}{2 \sin \theta_i} \right)^2 \cos^2 \phi + \left(\frac{\lambda R}{2VT} \right)^2 \sin^2 \phi \right] \quad (15)$$

in (11) to calculate the expected velocity spread since $K^2 A$ is more generally $(\vec{K} \cdot \vec{l})^2$ where $\vec{l} = (l_x, l_y)$ gives illuminated distances. Here c is the speed of light, τ_p is pulse length, R is range to the surface, and V is the velocity of the platform carrying the SAR. Note that if range and azimuth resolutions are equal, this reduces to the previous expression for A. We may examine the effects of integration time and R/V ratio on the velocity spread by using the spectral form deduced by *Donelan et al.* [1985] in (11) along with (15). Figure 15 shows the expected velocity spreads δv_r for $\delta v_o = 0.07$ m s^{-1}, $\tau_p = 10$ ns, $\theta_i = 45°$, a 50-km fetch, and the antenna looking perpendicular to the wave propagation direction. Curves for various combinations of T and $\lambda R/V$ are shown in Figure 15. Given these spreads of radial velocity, one can compute the coherence time to be used in SAR image modeling using (14).

Figure 16 shows the time/space filtering function which occurs because of the small size of the resolution cell and the finite integration time. This function is an integral over all wave directions of G times the angular part of the wave spectrum times the factor in brackets in (11); it has been normalized by its maximum value. Like the velocity spreads of Figure 15, it was computed using the spectrum of *Donelan et al.* [1985]. Since the angular spread of the wave spectrum varies with fetch and wind speed, the filtering function has a very slight dependence on these variables. In Figure 16, the wind speed is 12 m s^{-1} and the fetch is 50 km. As the figure shows, very long waves contribute little to the radial velocity spread and, therefore, to the correlation time. This is not to say that those longer waves do not contribute to the azimuthal falloff observed in spectra of SAR images of ocean waves, since velocity bunching contributes to this falloff in addition to the correlation time.

If the wind were not coming directly toward the antenna as was implicitly assumed by *Plant* [1991] and as was the case in this experiment, then the effect of Bragg splittings caused by advancing and receding Bragg-resonant waves would have to be taken into ac-

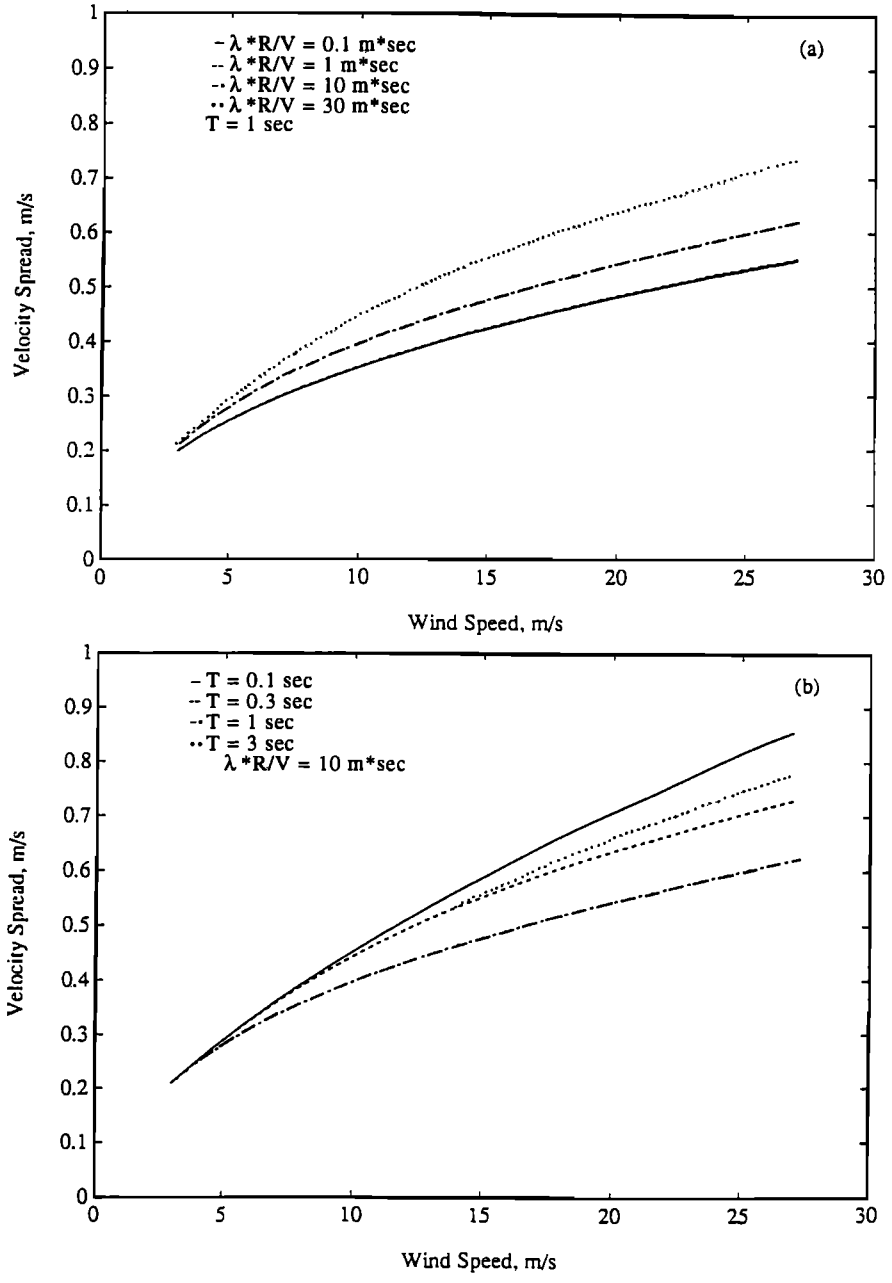

Figure 15. Predicted velocity spreads for SAR imagery of the ocean using the spectral model of *Donelan et al.* [1985]. Dominant wave propagation in the direction of flight, a 50-km fetch, and a 10-ns pulse width have been assumed. (a) T held constant, (b) $\lambda R/V$ held constant.

count [*Plant and Keller*, 1990]. It is easy to show that this effect causes the total velocity spread, δv_t, to be given by

$$\delta v_t = \delta v_r \left[1 + \frac{4c_B^2 \sigma_a \sigma_r \sin^2 \theta_i}{(\sigma_a + \sigma_r)^2 (\delta v_r)^2} \right]^{1/2} \tag{16}$$

where c_B is the Bragg wave phase speed, σ_a is the cross section of the advancing wave, and σ_r is the cross section of the receding wave. Since δv_r is usually on the order of c_B, this effect can potentially increase the velocity spread by 25% to 50% for winds with an appreciable azimuthal component.

The above considerations show that the radial velocity spread, and therefore the azimuthal rolloff exhibited by SAR imagery, will be a function of both the directional wave spectrum and the wind direction. Thus complex nonlinear effects that depend on surface conditions are introduced into the SAR image. These effects are in addition to the nonlinearities introduced by the modulation of the backscatter and, possibly, the Doppler bandwidth by long surface waves and the shift of the first moment of the Doppler spectrum with position on the long wave that is velocity bunching. In an accompanying paper we will examine the modulation of the cross section and Doppler bandwidth by long waves.

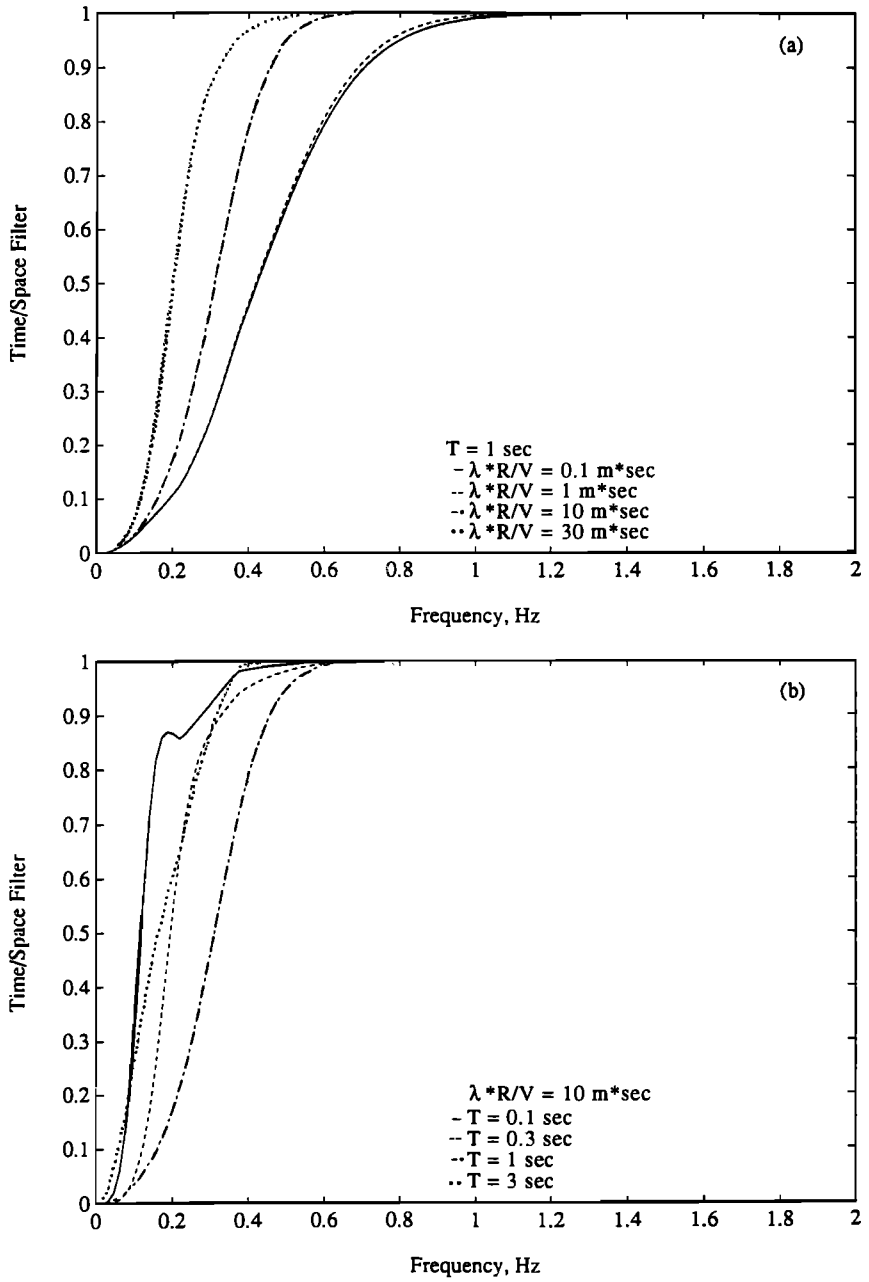

Figure 16. Time/space filter applied to ocean wave vertical velocity spectra in determining radial velocity spreads. An integral over wave direction has been performed, and the function has been normalized by its maximum value. (a) T held constant, (b) $\lambda R/V$ held constant.

That study along with the present paper provides many of the details of microwave backscatter from the ocean that are necessary to properly interpret SAR imagery of the ocean.

Acknowledgments. The authors would like to thank Peter Lobemeier of FWG for his logistical support during SAXON-FPN, for supplying us with meteorological data, and for his aid in arranging for the elevator to be constructed. We are grateful to RF for construction and mounting of the elevator. We also wish to thank Seigfried Stolte of FWG and David Arnold of MIT for their support with the meteorological data and Friedwart Ziemer of GKSS for supplying us with the directional wave spectra. Bruce Gotwols was very helpful throughout the experiments, especially with computer synchronizations and verification of the meteorological data. Maxine Jones and Ken Hayes supplied essential programming support for the project. The project was funded under grant number N00014-89-J-3224 from the Office of Naval Research.

References

Alpers, W., and K. Hasselmann, Spectral signal to clutter and thermal noise properties of ocean wave imaging synthetic aperture radars, *Int. J. Remote Sens.*, *3*(4), 423–446, 1982.

Alpers, W. R,. and C. L. Rufenach, The effect of orbital mo-

tions on synthetic aperture radar imagery of ocean waves, *IEEE Trans. Antennas Propag. (AP), 27*, 685–690, 1979.

Bass, F. G., I. M. Fuks, A. I. Kalmykov, I. E. Ostrovsky, and A. D. Rosenberg, Very high frequency radiowave scattering by a disturbed sea surface, 2, Scattering from an actual sea surface, *IEEE Trans. Antennas Propag. (AP), 16*, 560–568, 1968.

Donelan, M. A., J. Hamilton, and W. H. Hui, Directional spectra of wind-generated waves, *Philos. Trans. R. Soc. London Ser. A, 315*, 509–562, 1985.

Fischer, R. E., Standard deviation of scatterometer measurements from space, *IEEE Trans Geosci. Electron. (GE), 10*, 106–113, 1972.

Hasselmann, K., R. K. Raney, W. J. Plant, W. Alpers, R .A. Shuchman, D. R. Lyzenga, C. L. Rufenach, and M. J. Tucker, Theory of synthetic aperture radar ocean imaging: A MARSEN view, *J. Geophys. Res., 90*, 4659–4686, 1985.

Jakeman, E., and R. J. A. Tough, Non-Gaussian models for the statistics of scattered waves, *Adv. Phys., 37*, 471–529, 1988.

Kasilingam, D. P., and O. H. Shemdin, Theory for synthetic aperture radar imaging of the ocean surface: With application to the tower ocean wave and radar dependence experiment on focus, resolution and wave height spectra, *J. Geophys. Res., 93*, 13,837–13,848, 1988.

Lyzenga, D. R., An analytic representation of the synthetic aperture radar image spectrum for ocean waves, *J. Geophys. Res., 93*, 13,859–13,865, 1988.

Pidgeon, V. W., Time, frequency, and spatial correlation of radar sea return, *Rep. BPD-670-7*, pp. I1–I4, Appl. Phys. Lab., Johns Hopkins Univ., Laurel, Md., 1967.

Plant, W. J., The modulation transfer function: Concept and application, in *Radar Scattering from Modulated Wind Waves*, edited by G. J. Komen and W. A. Oost, pp. 155–172, Kluwer Academic, Norwell, Mass., 1989.

Plant, W. J., Bragg scattering of electromagnetic waves from the air/sea interface, in *Surface Waves and Fluxes*, edited by G. L. Geernaert and W. J. Plant, pp. 41–108, Kluwer Academic, Norwell, Mass., 1990.

Plant, W. J., The variance of the normalized radar cross section of the sea, *J. Geophys. Res., 96*, 20,643–20,654, 1991.

Plant, W. J., and W. C. Keller, The two-scale radar wave probe and SAR imagery of the ocean, *J. Geophys. Res., 88*, 9776–9784, 1983.

Plant, W. J., and W. C. Keller, Evidence of Bragg scattering in microwave doppler spectra of sea return, *J. Geophys. Res., 95*, 16,299–16,310, 1990.

Plant, W. J., W. C. Keller, E. A. Terray, and R. A. Petitt, Jr., Microwave backscatter from the sea: The modulation of received power and Doppler bandwidth by long waves, this issue.

Watts, S., and K. D. Ward, Spatial correlation in K-distributed sea clutter, *IEE Proceedings, 134*, 526–532, 1987.

Wright, J. W., A new model for sea clutter, *IEEE Trans. Antennas Propag. (AP), 16*, 217–223, 1968.

W. C. Keller and W. J. Plant, Applied Physics Laboratory, College of Ocean and Fishery Sciences, University of Washington, Seattle, WA 98105.

R. A. Petitt, Jr., and E. A. Terray, Woods Hole Oceanographic Institution, Woods Hole, MA 02543.

(Received August 24, 1992; revised March 30, 1993; accepted March 30, 1993.)